Quantum Hall effect and Landau level crossing of Dirac fermions in trilayer graphene
Supplementary Information

Thiti Taychatanapat[1], Kenji Watanabe[2], Takashi Taniguchi[2], Pablo Jarillo-Herrero[3]

[1] *Department of Physics, Harvard University, Cambridge, MA 02138, USA*

[2] *National Institute for Materials Science, Namiki 1-1, Tsukuba, Ibaraki 305-0044, Japan*

[3] *Department of Physics, Massachusetts Institute of Technology, Cambridge, MA 02139, USA*

Contents

S1. Fabrication process of graphene on hBN

We first spin polyvinyl alcohol (PVA) on an oxidized silicon substrate at 3000 rpm for 60 s and bake the chip at 75 °C for 4 minutes. We then spin Poly(methyl methacrylate) (PMMA) 950 A5 on top of PVA at 1500 rpm for 60 s and heat it at 75 °C for 10 minutes (Fig. S1a). Graphene is deposited on to the polymer stack by mechanical exfoliation (Fig. S1b and c). After exfoliation, the polymer stack is peeled off from the substrate and a graphene flake is identified using an optical microscope (Fig. S1d).

After we find the flake we want to transfer, we lay a washer atop the polymer film on the side opposite to the graphene flake. The washer acts as a support frame for the polymer film and is backed by a piece of tape to keep it in place (Fig. S1e and f). Since the washer is in between the polymer film and the tape, it prevents the polymer film from sticking to the tape. We then cut the tape into a small piece around the washer for transferring.
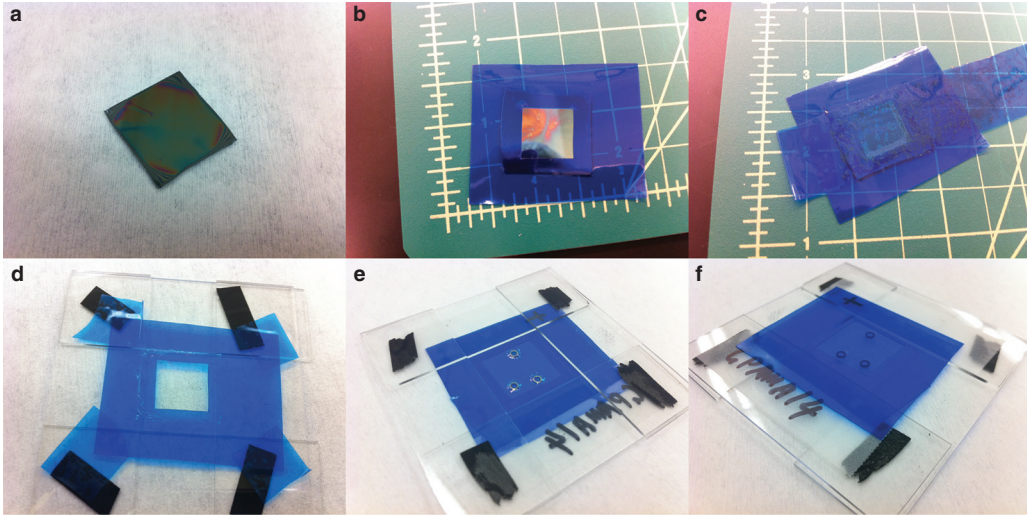

Figure S1: **Graphene transfer. a,** An oxidized silicon substrate covered by PVA and PMMA. **b,** The substrate is held in place by an acetone-soluble blue tape. This blue tape will later be used to peel off PVA and PMMA from the substrate. **c,** Graphene is mechanically exfoliated onto the polymer stack. **d,** The polymer stack (PVA and PMMA) with graphene on top is peeled off from the substrate. **e,** After identifying graphene, we put a washer around it and finally cover it by another tape. This allows us to use more than one piece of graphene per one preparation as opposed to a wet process in which only one graphene can be used. **f,** The back side of **e** showing another piece of tape used to cover the washers.

Similar to graphene, we prepare a thin sheet of hexagonal Boron Nitride (hBN) by mechanical exfoliation onto an oxidized silicon substrate (Fig. S2a). A potential hBN flake is identified by optical microscopy and we subsequently perform atomic force microscopy (AFM) to determine its roughness and thickness. We typically choose flakes with thickness less than 30 nm and without atomic steps/terraces. hBN flakes of
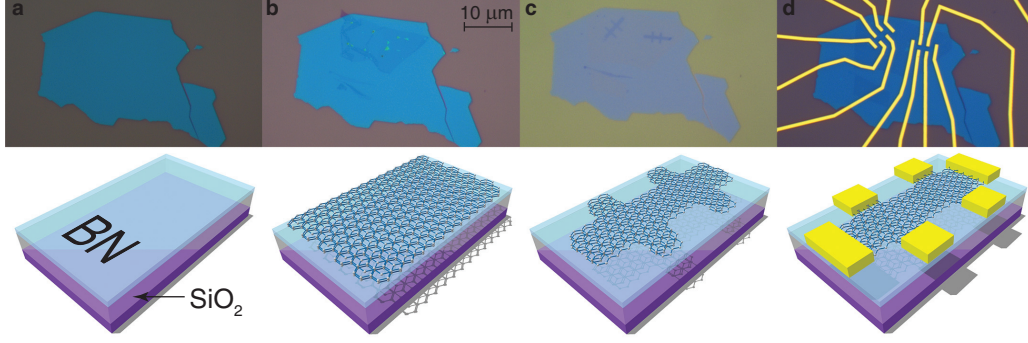
Figure S2: **Device Fabrication. a,** Hexagonal boron nitride is exfoliated onto an oxidized silicon substrate. **b,** A piece of graphene is transferred onto hBN. Ripples and bubbles, forming after the transfer process, can be seen in the optical image. **c,** Graphene is etched by oxygen plasma into hall bar geometry to avoid the ripples and bubbles. **d,** Contacts are defined by electron beam lithography and Cr and Au are deposited by thermal evaporation.

such thickness appear blueish under an optical microscope.

Once a graphene flake on a suspended polymer film and a hBN flake on SiO$_2$ are ready, we use a flip chip bonder to align the graphene flake to the hBN flake. Upon transferring, we heat up the substrate to 120 °C. We then press the polymer film onto the substrate for 5 minutes while keeping the temperature at 120 °C.

After the transfer process, often some areas of the graphene flake will have bubbles and/or ripples with smaller areas laying flat on hBN (Fig. S2b). To remove non-flat regions, we use PMMA as an etch mask and pattern a Hall bar geometry by standard electron beam lithography. Oxygen plasma etching is then used to etch uncovered graphene (Fig. S2c). After dissolving PMMA in acetone, we heat anneal the sample in forming gas (300 sccm of Ar and 700 sccm of H$_2$) to get rid of PMMA residue. The sample is heated up from room temperature to 350 °C for 1 hour and then held 350 °C for 2 more hours. After 2 hours, we turn off the heater and let the sample cool down slowly to room temperature. Contacts are then defined using electron beam lithography. We thermally evaporate 0.7 nm of Cr and 80 nm of Au, and lift off metals in acetone (Fig. S2d). We do a final heat annealing before cooling down the sample using the same recipe as above.

S2. Determination of SWMcC parameters

The hamiltonian for Bernal stacked TLG with SWMcC parameters is given by [S1]

$$H = \begin{bmatrix} H_m & D \\ D^\dagger & H_b \end{bmatrix},$$

where

$$D = \begin{bmatrix} \Delta_1 & 0 & 0 & 0 \\ 0 & 0 & 0 & \Delta_1 \end{bmatrix}, \quad H_m = \begin{bmatrix} \Delta_2 - \gamma_2/2 & v_0 \pi^\dagger \\ v_0 \pi & \Delta_2 - \gamma_5/2 + \delta \end{bmatrix},$$

$$H_b = \begin{bmatrix} \Delta_2 + \gamma_2/2 & \sqrt{2} v_3 \pi & -\sqrt{2} v_4 \pi^\dagger & v_0 \pi^\dagger \\ \sqrt{2} v_3 \pi^\dagger & -2\Delta_2 & v_0 \pi & -\sqrt{2} v_4 \pi \\ -\sqrt{2} v_4 \pi & v_0 \pi^\dagger & -2\Delta_2 + \delta & \sqrt{2} \gamma_1 \\ v_0 \pi & -\sqrt{2} v_4 \pi^\dagger & \sqrt{2} \gamma_1 & \Delta_2 + \gamma_5/2 + \delta \end{bmatrix}.$$

The SWMcC parameters γ_i for Bernal stacking TLG are shown in Fig. 1b with the corresponding effective velocity $v_i = (\sqrt{3}/2)a\gamma_i/\hbar$ and δ is the on-site energy difference between A and B sublattices. The parameters $\Delta_1 = (U_1 - U_3)/2$ and $\Delta_2 = (U_1 - 2U_2 + U_3)/3$ describe energy difference between layers where U_i is the potential of layer i. The basis for this hamiltonian is $(\psi_{A1} - \psi_{A3})/\sqrt{2}$, $(\psi_{B1} - \psi_{B3})/\sqrt{2}$, $(\psi_{A1} + \psi_{A3})/\sqrt{2}$, ψ_{B2}, ψ_{A2}, and $(\psi_{B1} + \psi_{B3})/\sqrt{2}$ which reflects the even and odd parity with respect to mirror symmetry of Bernal stacked TLG. We use this hamiltonian to calculate Landau levels numerically by rewriting $\pi^\dagger$ as $\sqrt{2\hbar eB} a^\dagger$ for K′ point and $\sqrt{2\hbar eB} a$ for K point respectively where $a^\dagger$ and a are creation and annihilation operators for simple harmonic oscillation [S2]. Figure S3 shows how the different parameters affect the band structure and LL energy spectrum.

To determine the SWMcC parameters, we set $\gamma_0 = 3.1$ eV which corresponds to $v_0 = 1 \times 10^6$ m/s [S3–S7] and $\gamma_1 = 0.39$ eV [S5, S8–S13]. We vary γ_2, γ_3, γ_4, γ_5 and δ and numerically determine the magnetic fields B^{t} and filling factors ν^{t} at which LL crossings occur. We then compare B^{t} and ν^{t} with the crossing points observed experimentally. Twelve crossing points can be resolved in the data (Fig. 2, S4 and Table S1). The best set of SWMcC parameters is the one which yields the correct ν^{t} and the minimum value of

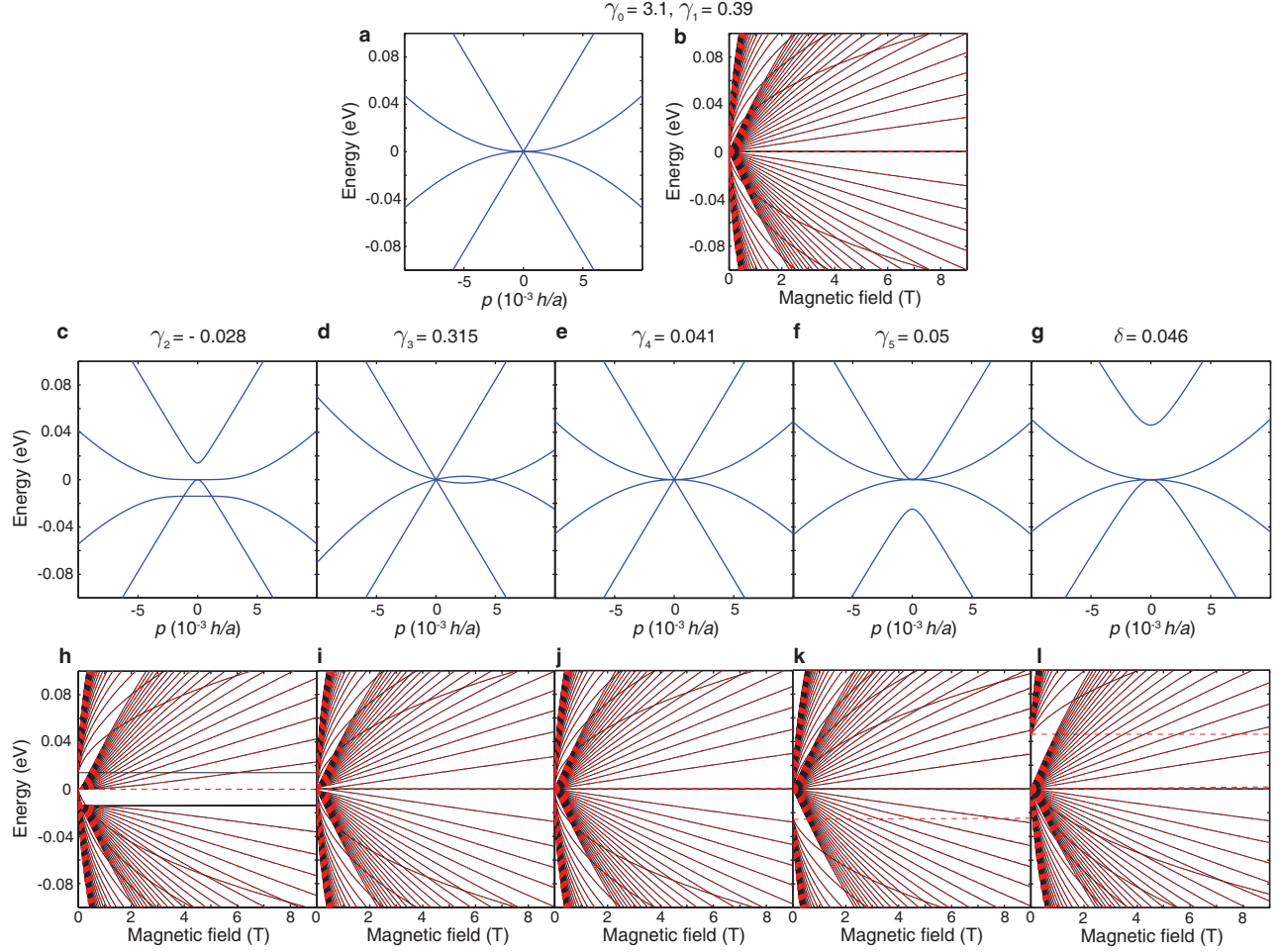$$\xi = \sum_{i=1}^{12} \left(\frac{B_i^{\mathrm{t}} - B_i^{\mathrm{exp}}}{\Delta B_i^{\mathrm{exp}}} \right)^2,$$

4

Figure S3: **Dependence of TLG band structure and Landau levels on the SWMcC parameters. a-b,** Band structure and Landau levels of TLG with $\gamma_0 = 3.1$ eV and $\gamma_1 = 0.39$ eV. **c-l,** Band structure and Landau levels of TLG with nonzero γ_i (shown on top of each plot) and $\gamma_0 = 3.1$ eV and $\gamma_1 = 0.39$ eV.

where B_i^{exp} and $\Delta B_i^{\mathrm{exp}}$ are the values of magnetic field and their uncertainties at the crossing points, determined experimentally (Fig. 2 and S4). In addition, according to the data at 9 T (Fig. 4), in which we observe the quantized conductance at $\nu = 4$ but not at $\nu = 6$, we require that the energy gap at $\nu = 4$ has to be larger than the gap at $\nu = 6$.

We find that the positions of the crossing points depend much more strongly on γ_2, γ_5, and δ than on γ_3 and γ_4 (see Fig. S3. In fact, the crossing points are almost not affected by γ_3. This is because the effect of γ_3 on the band structure is to introduce trigonal warping in the bilayer-like subband at very low energies. This trigonal warping causes only a slight change in the very low-lying LLs at low magnetic field [S14], and these are not well resolved in our data (Fig. 2 and Fig. S7), which prevents us from using those LL

Table S1: **Magnetic fields and filling factors at which LL crossings occur.** We determine B^{exp} from the position of magnetic field at which σ_{xx} is locally maximum (data not shown).

N^{th} LL$_{\text{S}}$	N^{th} LL$_{\text{B}}$	ν^{exp}	B^{exp} (T)
-1	-5	-26	7.31
-1	-6	-30	3.04
-2	-11	-54	3.07
-2	-12	-58	2.09
-3	-16	-78	2.57
-3	-17	-82	1.98
-3	-18	-86	1.51
-4	-22	-106	1.78
-4	-23	-110	1.44
-5	-27	-130	1.56
-5	-28	-134	1.35
0	6	23	1.75

crossings in our fitting procedure. Therefore we set γ_3 to a fixed value of 0.315 eV [S8], and vary γ_2, γ_4, γ_5, and δ. We obtain $\gamma_2 = -0.028(4)$ eV, $\gamma_4 = 0.041(10)$ eV, $\gamma_5 = 0.05(2)$ eV, and $\delta = 0.046(10)$ eV. Our data cannot determine γ_5 and δ individually accurately because we can access only the low lying term $-\gamma_5/2+\delta$ in the hamiltonian while the other term $\gamma_5/2+\delta$ is much higher in energy due to the hybridization through the nearest inter-layer coupling γ_1. However, we can determine $-\gamma_5/2+\delta$ with better accuracy and obtain $-\gamma_5/2 + \delta = 0.021(3)$ eV.

We note that we have set $\Delta_1 = 0$ and $\Delta_2 = 0$. The effect of Δ_1 is to hybridize the SLG-like and BLG-like subbands, which lifts two of the four low energy subbands to higher energy. Δ_2 induces a small gap in the BLG-like subband. It is reasonable to set $\Delta_2 = 0$ because, in a linear response calculation, Δ_2 is always zero and, using a self-consistent calculation, Δ_2 is still less than 1 mV [S1]. However, the value of Δ_1 could be as high as 50 mV at the density of $\sim 4 \times 10^{12}$ cm^{-2} (~ 60 V in back gate voltage) which we access experimentally [S1]. Such value of Δ_1 should affect the LL spectrum, and therefore the crossing points, very strongly. However, we were unable to find a set of SWMcC parameters which would describe our crossing points for values of Δ_1 larger than about 10 meV, and the agreement was best for values of Δ_1 equal to zero.
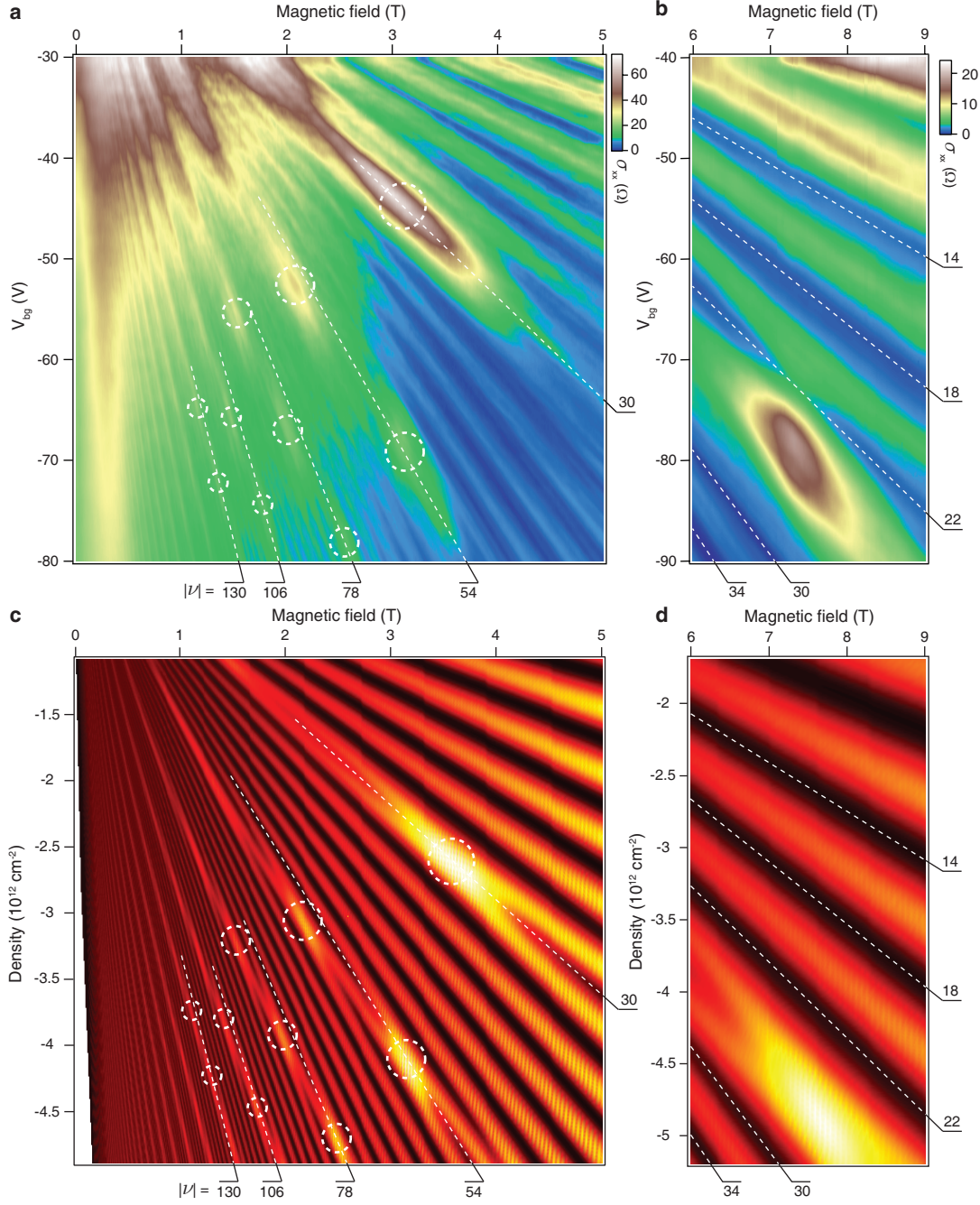
Figure S4: **Landau fan diagram. a,** Color map of Landau fan diagram as a function of back-gate voltage and magnetic field at 300 mK. White dashed lines are guides to the eye with filling factors labeled on the edge and the white dashed circles indicate crossing points. **b,** Landau fan diagram from 6 to 9 T at 300 mK. The measurement is taken when the sample quality is not high enough to observe LL splitting (Fig. 3a). The absence of the minimum at $\nu = -26$ can be seen clearly indicating Landau level crossing. **c,** Calculated DOS as a function of density and magnetic field. Here we use $\Gamma = 1$ mV and the following SWMcC parameters: $\gamma_0 = 3.1$ eV, $\gamma_1 = 0.39$ eV, $\gamma_2 = -0.028$ eV, $\gamma_3 = 0.315$ eV, $\gamma_4 = 0.041$ eV, $\gamma_5 = 0.05$ eV, and $\delta = 0.046$ eV. **d,** Calculated DOS as a function of density and magnetic field with $\Gamma = 2.5$ mV and the same SWMcC parameters as in **c.**
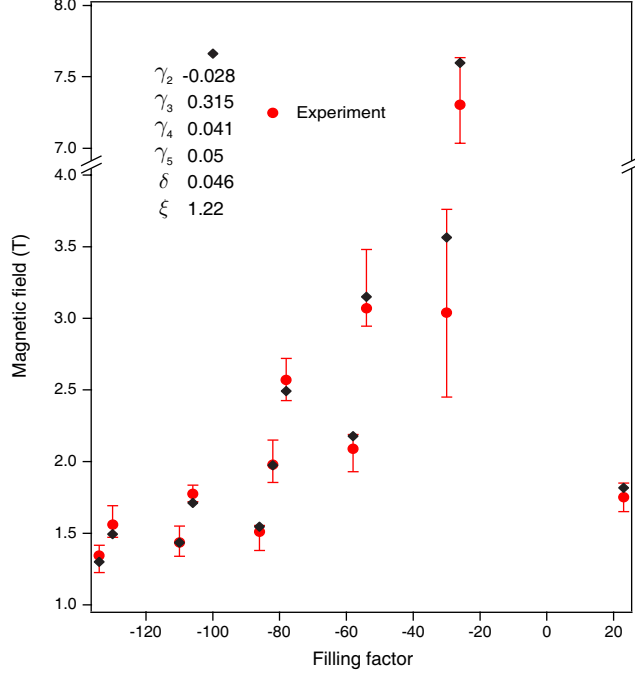
7

Figure S5: **Crossing coordinates.** The positions of the crossing points in magnetic field and filling factor for different sets of parameters. The red circles are the positions of the crossing points determined experimentally.

The naive picture of using a single value of Δ_1 to describe the data at all densities is clearly not sufficient, because Δ_1 depends on the carrier density we induce in the system via the back gate voltage. However, the calculation of LL spectrum with density-dependent Δ_1 is much more involved, and requires a self consistent calculation, beyond the scope of this paper. The fact that we can reproduce the experimentally observed LL crossing points with $\Delta_1 = 0$ may imply that high mobility TLG can screen electric field very well at high densities (where the LL crossing points are measured), causing the potential of each layer to be similar.

After obtaining the Landau level spectrum, we calculate the density of states (DOS) by assuming that the DOS of each Landau level is of the form

$$\mathrm{DOS}(E; E_{\mathrm{LL}}) = \frac{2B}{h/e} \frac{1}{\pi} \frac{\Gamma/2}{(E - E_{\mathrm{LL}})^2 + (\Gamma/2)^2},$$

where E_{LL} is the energy of the LL and Γ is the broadening of the LL due to disorder. The factor of 2 in front comes from spin degeneracy. We calculate the LL spectrum separately for K and K′ because of their

non degeneracy. The total DOS can be obtained by summing over the DOS of each Landau level

$$\mathrm{DOS}_{\mathrm{total}}(E) = \sum_{E_{\mathrm{LL}}} \mathrm{DOS}(E; E_{\mathrm{LL}}).$$

We then integrate total DOS in order to obtain the DOS as a function of density and B which can be used to compare with the experimental data. Figure S6 shows the different LL energy spectra and fan diagrams for the SWMcC parameters for graphite from different sources (see Table S2), and the comparison with the spectrum and fan diagram for the SWMcC parameters for TLG obtained in this work.
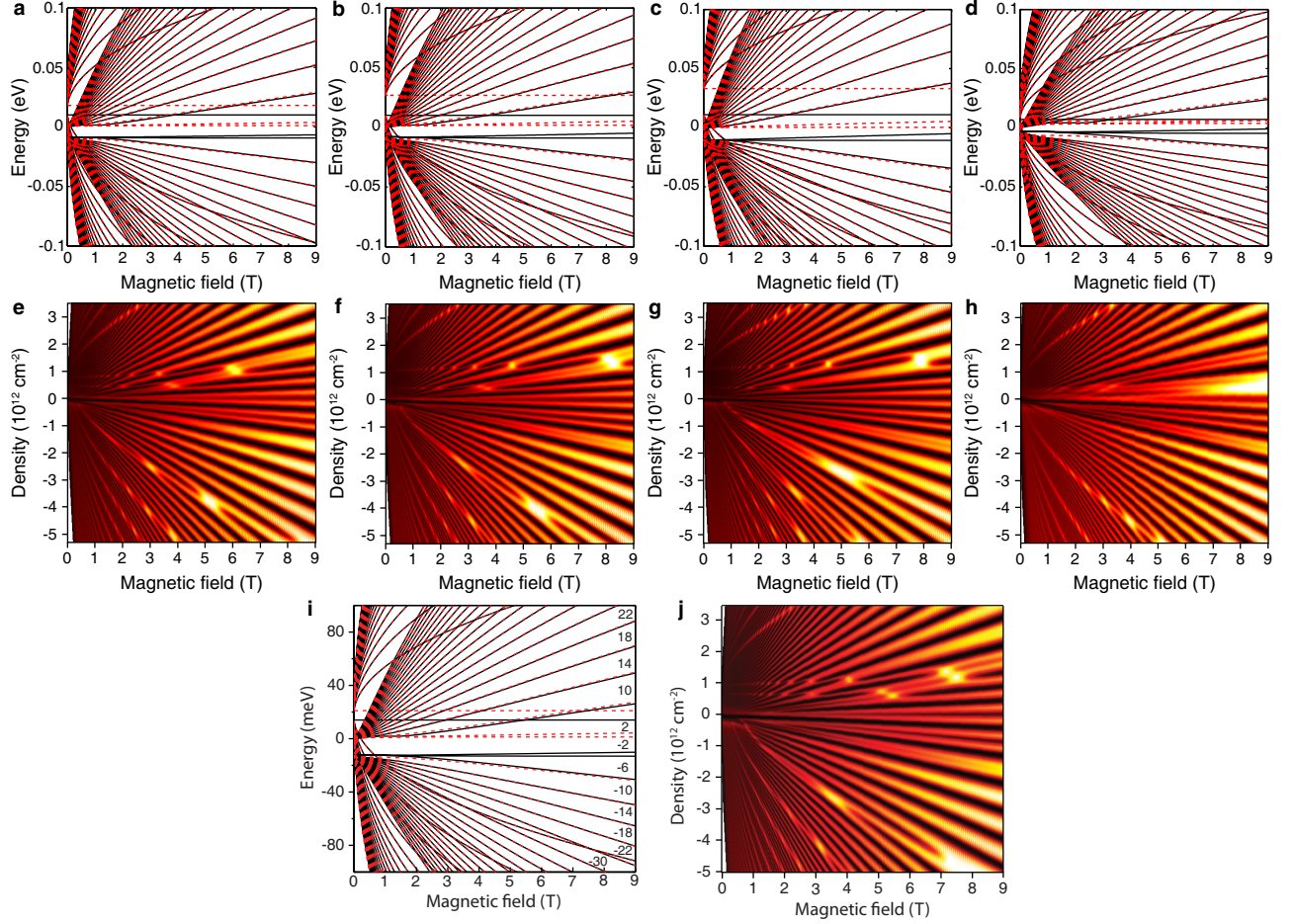

Figure S6: **Landau fan diagrams with SWMcC parameters from graphite. a-d,** Landau level energy spectrum as a function of magnetic field using the SWMcC parameters determined from graphite from references [S8], [S15], [S16], and [S17] respectively (Table S2). Red and black curves represent Landau level from K and K′. **e-f,** Density of states as a function of magnetic field and density calculated from the energy spectrum in **a**, **b**, **c**, and **d** respectively. Figures **e** and **f** looks similar to our data but the crossing point at high field ($\sim$5 T) occurs at $\nu = 30$ instead of $\nu = 26$ observed experimentally. **i-j,** Landau level energy spectrum and density of states using the SWMcC parameters from our TLG data.

Table S2: **SWMcC parameters.** SWMcC parameters obtained from fitting the positions of the LL crossings are shown in row 1. The parameters obtained previously on graphite by means of experiment (Exp) and density functional theory (DFT) are listed in rows 2 to 4. In the last row, the parameters for BLG as determined by infrared spectroscopy. We note that γ_2 and γ_5, which describe the hopping between the first and the third layers, are not present in BLG. Rows 2-5 of this table are adopted from Zhang *et al* [S11].

Source	γ_0	γ_1	γ_2	γ_3	γ_4	γ_5	δ
TLG (Pres. Result)	$3.1^{\dagger}$	$0.39^{\dagger}$	-0.028(4)	$0.315^{\dagger}$	0.041(10)	0.05(2)	0.046(10)
Graphite Exp [S8]	3.16(5)	0.39(1)	-0.020(2)	0.315(15)	0.044(24)	0.038(5)	0.037(5)
Graphite Exp [S15]	3.11	0.392	-0.0201	0.29	0.124	0.0234	0.0386
Graphite DFT [S16]	2.92	0.27	-0.022	0.15	0.10	0.0063	0.0362
Graphite DFT [S17]	2.598(15)	0.364(20)	-0.014(8)	0.319(20)	0.177(25)	0.036(13)	0.024(18)
BLG [S11]	3.0	0.40(1)	0.0	0.3	0.15(4)	0.0	0.018(3)

† The values of γ_0 and γ_1 are taken from literature where the reported values from different experiments have been consistent. The value of γ_3 cannot be determined accurately and hence is taken from ref. [S8].
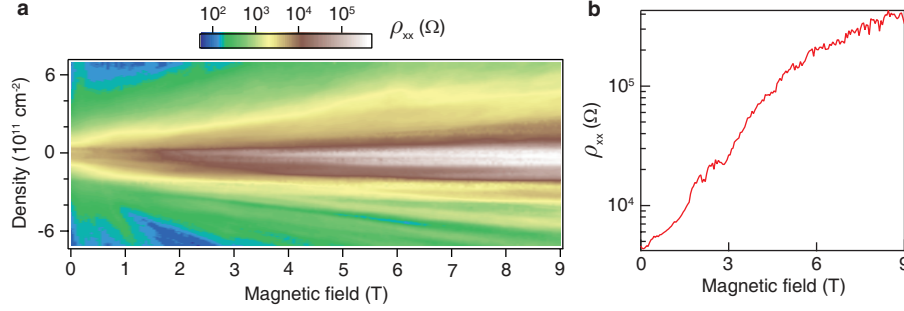
Figure S7: **Landau fan diagram at $\nu = 0$. a,** Color map of ρ_{xx} versus density and B at 300 mK. **b,** A slice from **a** at zero density.

S3. Insulating behavior at $\nu = 0$

We observe an insulating behavior in ρ_{xx} at zero density as we increase B. The longitudinal resistivity ρ_{xx} increases from $4.5\,\mathrm{k\,\Omega}$ at 0 T to $400\,\mathrm{k\,\Omega}$ at 9 T. This insulating behavior at $\nu{=}0$ is also observed in SLG and BLG [S18–S21]. In those systems, electron-electron interactions are required to break the symmetry of the zero energy LL. In TLG, due to the finite values of γ_2, γ_5, and δ, which cause valley splitting in the SLG- and BLG-like subbands LLs as well as breaking of the $N = 0$ and 1 LLs in BLG-like subband, there are no LLs at zero density. In general, the valley degeneracy is associated with a spacial inversion symmetry which is present in both SLG and BLG. However, Bernal stacked TLG does not preserve spatial inversion symmetry and hence the valley degeneracy is not guaranteed [S22]. However, the finite band overlap implies that there should be edge modes present always, for any value of the Fermi energy (or density) [S23]. Therefore, electron-electron interactions may play a role in this insulating behavior. Note that this insulating phase has also been observed in a suspended TLG sample [S24].

References

[S1] Koshino, M. & McCann, E. Gate-induced interlayer asymmetry in ABA-stacked trilayer graphene. *Phys. Rev. B.* **79**, 125443 (2009).

[S2] Koshino, M. & McCann, E. Trigonal warping and Berry's phase $N\pi$ in ABC-stacked multilayer graphene. *Phys. Rev. B* **80**, 165409 (2009).

[S3] Novoselov, K. S. *et al.* Two-dimensional gas of massless Dirac fermions in graphene. *Nature* **438**, 197–200 (2005).

[S4] Zhang, Y., Tan, Y.-W., Stormer, H. L. & Kim, P. Experimental observation of the quantum Hall effect and Berry's phase in graphene. *Nature* **438**, 201–204 (2005).

[S5] Li, G. & Andrei, E. Y. Observation of Landau levels of Dirac fermions in graphite. *Nature Phys.* **3**, 623–627 (2007).

[S6] Miller, D. L. *et al.* Observing the quantization of zero mass carriers in graphene. *Science* **324**, 924–927 (2009).

[S7] Song, Y. J. *et al.* High-resolution tunnelling spectroscopy of a graphene quartet. *Nature* **467**, 185–189 (2010).

[S8] Dresselhaus, M. S. & Dresselhaus, G. Intercalation compounds of graphite. *Adv. Phys.* **51**, 1–186 (2002).

[S9] Ohta, T., Bostwick, A., Seyller, T., Horn, K. & Rotenberg, E. Controlling the electronic structure of bilayer graphene. *Science* **313**, 951–954 (2006).

[S10] Yan, J., Henriksen, E. A., Kim, P. & Pinczuk, A. Observation of anomalous phonon softening in bilayer graphene. *Phys. Rev. Lett.* **101**, 136804 (2008).

[S11] Zhang, L. M. *et al.* Determination of the electronic structure of bilayer graphene from infrared spectroscopy. *Phys. Rev. B* **78**, 235408 (2008).

[S12] Li, Z. Q. *et al.* Band structure asymmetry of bilayer graphene revealed by infrared spectroscopy. *Phys. Rev. Lett.* **102**, 037403 (2009).

[S13] Kuzmenko, A. B., Crassee, I., van der Marel, D., Blake, P. & Novoselov, K. S. Determination of the gate-tunable band gap and tight-binding parameters in bilayer graphene using infrared spectroscopy. *Phys. Rev. B* **80**, 165406 (2009).

[S14] McCann, E. & Fal'ko, V. L. Landau-level degeneracy and quantum Hall effect in a graphite bilayer. *Phys. Rev. Lett.* **96**, 086805 (2006).

[S15] Dillon, R., Spain, I. & McClure, J. Electronic energy band parameters of graphite and their dependence on pressure, temperature and acceptor concentration. *J. Phys. Chem. Solids* **38**, 635 – 645 (1977).

[S16] Tatar, R. C. & Rabii, S. Electronic properties of graphite: A unified theoretical study. *Phys. Rev. B* **25**, 4126–4141 (1982).

[S17] Charlier, J.-C., Gonze, X. & Michenaud, J.-P. First-principles study of the electronic properties of graphite. *Phys. Rev. B* **43**, 4579–4589 (1991).

[S18] Zhang, Y. *et al.* Landau-level splitting in graphene in high magnetic fields. *Phys. Rev. Lett.* **96**, 136806 (2006).

[S19] Feldman, B. E., Martin, J. & Yacoby, A. Broken-symmetry states and divergent resistance in suspended bilayer graphene. *Nature Phys.* **5**, 889–893 (2009).

[S20] Zhao, Y., Cadden-Zimansky, P., Jiang, Z. & Kim, P. Symmetry breaking in the zero-energy Landau level in bilayer graphene. *Phys. Rev. Lett.* **104**, 066801 (2009).

[S21] Dean, C. R. *et al.* Boron nitride substrates for high-quality graphene electronics. *Nature Nanotech.* **5**, 722–726 (2010).

[S22] Koshino, M. & McCann, E. Parity and valley degeneracy in multilayer graphene. *Phys. Rev. B* **81**, 115315 (2010).

[S23] Abanin, D. A. *et al.* Dissipative quantum hall effect in graphene near the dirac point. *Phys. Rev. Lett.* **98**, 196806 (2007).

[S24] Bao, W. *et al.* Magnetoconductance oscillations and evidence for fractional quantum Hall states in suspended bilayer and trilayer graphene. *Phys. Rev. Lett.* **105**, 246601 (2010).